Global NEST Journal, Vol 28, No X, pp 1-16

N,Fe-doped carbon dots/UV synergistically accelerated Fe^{3+}/Fe^{2+} cycle for Peroxymonosulfate activation to degrade carbamazepine: Degradation performance, mechanisms, and toxicity assessment

Weiwei Yu[A*#], Beiyan Li[A#], Sikai Zhao[A], Chuandong Tang[B], Bolin Li[C], Feng Yu[A], Yuanxin Liu[A], Ji Li[A], Xinyan Li[A], Dan Liu[A] and Yan Luo[A]

[A]Key Laboratory of Hydraulic and Waterway Engineering of the Ministry of Education, School of River and Ocean Engineering, Chongqing Jiaotong University, No.66 Xuefu Rd., Nan'an Dist., Chongqing 400074, China

[B]China Academy of Urban Planning & Design Western Branch, ChongQing, 401121, China

[C]School of Resource and Environmental Engineering, Wuhan University of Technology, Wuhan, Hubei Province 430070, China

[#] These authors are co-first authors of the article.

Received: 26/11/2025, Accepted: 22/01/2026, Available online: 09/02/2026

*to whom all correspondence should be addressed: e-mail: yu11237@cqjtu.edu.cn

https://doi.org/10.30955/gnj.08229

Graphical abstract

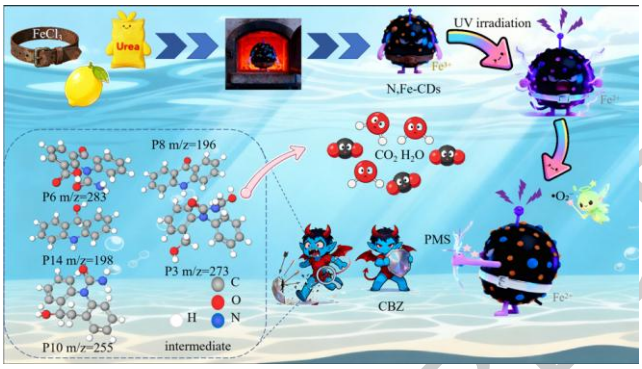

Abstract

Nitrogen- and iron-co-doped carbon dots (N,Fe-CDs) were synthesized via a hydrothermal method and rationally engineered as a low-iron, UV-responsive catalyst in a UV/N,Fe-CDs/peroxymonosulfate (PMS) system for rapid carbamazepine (CBZ) degradation. Characterization verified a near-spherical morphology, with iron chelation improving light absorption, electron transfer, and catalytic stability. Fe–O, Fe–N, and Fe–OH coordination stabilized Fe species and promoted Fe(III)/Fe(II) redox cycling under UV irradiation through photoinduced electron transfer and ligand-to-metal charge transfer (LMCT). This ensured that the process performed successfully in a large range of PH, between 3 and 9. When the right conditions were met (0.5 mM PMS, 0.10 g/L N,Fe-CDs), 95.4% of the CBZ was removed in 20 minutes, which was 6.8 times faster than UV/PMS. Ions that were present at the same time, like Mg^{2+}, NH_4^+, Cl^-, and HCO_3^- , greatly slowed down degradation. SO_4^{2-} only slowed it down at high concentrations, whereas NO_3^- and humic acid had little effect. Mechanistic studies identified $^1O_2$ and $\bullet O_2^-$ as the main species, while $SO_4\bullet^-$ and •OH were less important. HPLC-MS/MS found 14 intermediates, and density functional theory calculations pointed to hydroxylation and ring-opening of the seven-membered heterocycle as the main ways these things happen. Predictions of toxicity showed lower risks to the environment. Overall, the UV/N,Fe-CDs/PMS system couples Fe coordination stabilization with UV-assisted PMS activation, suggesting promise for wastewater treatment in complex matrices.

Keyword: N,Fe-doped carbon dots; Fe^{3+}/Fe^{2+} cycling; Peroxymonosulfate activation; Carbamazepine degradation

1. Introduction

Carbamazepine (CBZ) is a widely used aromatic pharmaceutical containing a nitrogen heterocycle and is one of the most frequently detected PPCPs in aquatic environments. Clinically, CBZ is prescribed for neuropathic pain, epilepsy, and bipolar disorder (Almeida *et al.* 2021). Its global consumption has continued to increase, with annual usage estimated at 1014 tons (Zhang *et al.* 2008). Approximately 72% of orally ingested CBZ is absorbed, while the unmetabolized fraction (~28%) is excreted and enters sewage systems (Brezina *et al.* 2017). Consequently, CBZ residues have been reported in wastewater treatment plant effluents and surface waters at 460–6300 ng/L and 263–11561 ng/L, respectively, and up to 610 ng/L in drinking water (Wang *et al.* 2020). Current treatment technologies usually fail in case of an accident or unexpected release of pharmaceuticals, endangering water habitats (Chen *et al.* 2017). Therefore, developing effective and environmentally benign strategies for rapid CBZ removal is a high priority.

High mineralization proofs of recalcitrant pollutants are documented in methodologies of advanced oxidation

Weiwei Yu, Beiyan Li, Sikai Zhao, Chuandong Tang, Bolin Li, Feng Yu, Yuanxin Liu, Ji Li, Xinyan Li, Dan Liu and Yan Luo (2026), N, Fe-doped carbon dots/UV synergistically accelerated Fe^{3+}/Fe^{2+} cycle for Peroxymonosulfate activation to degrade carbamazepine: Degradation performance, mechanisms, and toxicity assessment, *Global NEST Journal*, **28**(XX), 1-16.

(AOPs), such as ozone, hydroxyl-radical-binding oxidation, and UV-assisted oxidation (Gholizade *et al.* 2023). In particular, sulfate-radical (SO_4•–) AOPs have gained prominence due to their high redox potential and selectivity (Cai *et al.* 2021; Zeng *et al.* 2022). UV activation of peroxymonosulfate (PMS) directly yields SO_4•– and has been applied to degrade diverse contaminants (Li, H. *et al.* 2022; Ling *et al.* 2023). Nevertheless, standalone UV/PMS suffers from high energy/chemical demand, largely limited by the modest PMS light absorption and quantum yield (Ling *et al.* 2017).

Iron-activated PMS systems can effectively remove recalcitrant organics through the combined action of SO_4•$^-$, •OH and high-valent Fe(IV). However, Fe(II)/PMS often requires high Fe(II) dosages because Fe(II) regeneration is slow, increasing cost and sludge formation (Dong *et al.* 2021; Wang *et al.* 2022). Precipitation of Fe(III) at pH > 3 further suppresses catalysis (Stefánsson 2007). Under irradiation, Fe(III) can be photoreduced to Fe(II), improving radical production. Ahmed *et al.* demonstrated that UV-Vis/PMS/Fe(II) degraded pesticides and pharmaceuticals at rates an order of magnitude higher than UV-Vis/TiO_2 (Ahmed *et al.* 2014); likewise, Fe^{2+} addition enhanced UV-C/PMS removal of seven PhACs with the highest TOC reduction in PMS/Fe(II)/UV-C (Rodríguez-Chueca *et al.* 2019). These findings motivate designs that stabilize iron, accelerate Fe(III)/Fe(II) cycling, and sustain activity at mildly acidic to neutral pH.

Carbon dots (CDs), as a novel carbon nanomaterial composed of a carbon core and passivated surface, offer advantages such as economical synthesis raw materials, diverse preparation methods (including the commonly used hydrothermal method in laboratories), and controllable fabrication processes (Rahmani and Ghaemy 2019; Wang and Hu 2014; Zhang *et al.* 2022). Synthesis conditions allow precise tuning of their physicochemical properties. Taking advantage of their peculiar structure, CDs have excellent optical characteristics, excellent water solubility, biocompatibility, photostability, and easy surface modification (Lim *et al.* 2015; Rosso *et al.* 2020). Under illumination, CDs can store and shuttle photoexcited electrons, making them promising mediators in photochemical reactions (Di *et al.* 2015). Usually, the Fe(III)/Fe(II) cycle is among the fundamental reactions of the advanced oxidation process (AOPs) in carbon materials iron-doped (Zhao, G. *et al.* 2021). Studies have shown that the iron-doped biochar is an electron donor-acceptor medium in the treatment of organic pollutants. It increases the density and reactivity of surface-active sites, facilitating Fe(III) reduction and enhancing Fe(III)/Fe(II) cycling, thereby stabilizing iron species and sustaining catalytic activity (Ahmad *et al.* 2023). In addition, by covalently attaching heteroatoms (e.g. N, P, S) into the carbon skeleton, electron density and local structure can be regulated to improve the capacity of Fe(III) to capture electrons. Therefore, N-doped CDs drastically enhance light absorption and electron storage/transfer properties (Shi *et al.* 2017; Wang *et al.* 2017); The acquisition of a transition metal Fe is capable of binding with the functional groups of the CDs and demonstrates an excellent catalytic effect (Bourlinos *et al.* 2017). Multi-heteroatomic co-doping has become a focus instead of the single-atom doping because it allows them to cause synergistic effects resulting in unique electronic structures (Miao *et al.* 2020). Given the low cost and environmental friendliness of CDs, it is necessary to design and study N,Fe-CDs to optimize catalytic degradation systems.

The Fe,N-CDs/PMS system was able to efficiently activate PMS to generate free radicals in a wider pH range, thus effectively promoting the degradation of CBZ. This capability was corroborated by Yang *et al.* (Yang *et al.* 2024) who showed that under visible light irradiation and in a wide pH range of 5-9, the Fe,N-CDs/RF composites exhibited significantly enhanced photocatalytic activity compared to the baseline RF materials, achieving a 3.2-fold increase in the rate constant (k) for the degradation of chloroquine phosphate (CQ). Therefore, this study aims to (1) synthesize stable N,Fe co-doped carbon dots (N,Fe-CDs) via the hydrothermal method to stabilize iron ions, address the issue of slow iron cycling at pH > 3, and provide photoelectrons under UV light to accelerate iron cycling, thereby constructing a UV/N, Fe-CDs/PMS degradation system, achieving multi-pathway synergistic activation of the PMS process through the lower iron content in N,Fe-CDs, significantly enhancing the degradation performance of CBZ, and systematically investigating the key factors influencing CBZ degradation efficiency (such as catalyst dosage, PMS concentration, pH value, coexisting substances, etc.); (2) identify the dominant reactive species in the UV/N,Fe-CDs/PMS system and elucidate how surface Fe(III)/Fe(II) redox cycling drives PMS activation and CBZ degradation; meanwhile, by comparing light and dark conditions and tracking ROS signatures, we will verify that UV irradiation is indispensable for reactive species generation and sustained Fe cycling. Combining the identification of target degradation products, key reaction intermediates, and DFT calculations, propose possible degradation pathways for CBZ; (3) Evaluate the ecological toxicity of degradation intermediates to ensure the environmental safety of the degradation system. The N,Fe-CDs/PMS composite oxidation system developed in this study provides an effective emergency response strategy for addressing accidental leaks of carbamazepine pharmaceutical wastewater and elucidates the degradation behavior of CBZ in a PMS catalytic oxidation system based on carbon dots from a mechanistic perspective.

2. Materials and methods

2.1. Chemicals and reagents

Carbamazepine ($C_{15}H_{12}N_2O$) was purchased from Aladdin (Shanghai, China). Citric acid monohydrate ($C_6H_8O_7$-H_2O), urea (CH_4N_2O), ferric chloride ($FeCl_3$-$6H_2O$), potassium peroxydisulfate ($2KHSO_5$-$KHSO_4$-K_2SO_4), 1,10-o-phenanthroline ($C_{12}H_8N_2$), ferrous ammonia sulfate ($Fe(NH_4)_2(SO_4)_2$-$6H_2O$), hydroxylamine hydrochloride (ClH_4NO), ammonium acetate ($C_2H_7NO_2$), and hydroxyamine hydrochloride (ClH_4NO). Ammonium

Acetate ($C_2H_7NO_2$), glacial acetic acid ($C_2H_4O_2$), hydrochloric acid (HCl), sodium hydroxide (NaOH), sodium thiosulfate ($NA_2S_2O_3$), sodium chloride (NaCl), sodium hydrogen carbonate ($NaHCO_3$), sodium nitrate ($NaNO_3$), sodium sulfate (Na_2SO_4), calcium sulfate ($CaSO_4$), magnesium sulfate ($MgSO_4$), ammonium sulfate ($(NH_4)_2SO_4$) were purchased from Sinopharm Chemical Reagent (Shanghai, China).Tert-butanol ($C_4H_{10}O$), p-benzoquinone ($C_6H_4O_2$), furfuryl alcohol ($C_5H_6O_2$), methanol (CH_3OH), acetonitrile (CH_3CN), humic acid (HA) were purchased from Maclean's (Shanghai, China). All chemicals were analytically pure and deionized water was used in this study.

2.2. Preparation and characterization of materials

2.2.1. Preparation of N,Fe-CDs

N,Fe-CDs were prepared by a facile hydrothermal method. Citric acid 6.0 mmol monohydrate and 2.0 mmol ureawere added to 20 mL ultrapure water and dissolved under stirring at room temperature. Subsequently, 0.5 mmol of ferric chloride hexahydrate was added to the solution with continuous stirring to ensure that the components were fully reacted. The resulting solution was transferred to a Teflon-lined stainless-steel autoclave, sealed, and heated at 180 °C for 8 h. After cooling to room temperature, the reaction product was filtered using an aqueous filter membrane with a pore size of 0.22 μm to remove insoluble impurities. The filtrate was dialyzed using a dialysis bag with a MWCO of 1000 Da for 6 h to further purify the product. Finally, the dialysate was freeze-dried to obtain N,Fe-CDs in brown powder form.

2.2.2. Characterization of the material

The morphological structure of N,Fe-CDs was observed using TEM (FEI TALOS-F200X). Chemical composition was analyzed by Fourier transform infrared spectroscopy (FTIR, Nicolet IS5) in transmission mode (400-4000 cm^{-1}). Crystal structure was determined via X-ray diffraction (XRD, Bruker D8 Advance) using Fe Kα radiation (40 kV, 40 mA) with a scanning range of 10-80° (2θ) at 5°/min. X-ray photoelectron spectroscopy (XPS, Thermo K-Alpha) with Al Kα source (1486.68 eV) examined surface composition (0-1300 eV range). UV-Vis absorption spectra (200-600 nm) were recorded using a Shimadzu UV-3600 spectrophotometer. Photoelectrochemical properties were evaluated using a CHI 660E workstation with a three-electrode system (Ag/AgCl as reference electrode, platinum electrode as the counter electrode, and a sample-coated conductive glass as working electrode) in 0.5 M Na_2SO_4 electrolyte, with transient photocurrent responses measured under alternating dark/light conditions.

2.3. Degradation experiment

A low-pressure mercury lamp (λ=254 nm, power 10 W) with an external quartz sleeve was used as the UV light source, which was placed on the magnetic stirrer and immersed into the quartz container, and the reaction was started after 30 mins of preheating to ensure that the intensity of radiation was stabilized at 28 μW/cm². During the reaction, the temperature was controlled by air cooling and the magnetic stirrer's own heating system. 200 mL of carbamazepine solution was poured into a 300 mL quartz beaker, and a preset amount of PMS and catalytic material was added under light-avoidance conditions, and the magnetic thermostat stirrer was activated to carry out stirring for 30 min to ensure the adsorption-desorption equilibrium. Subsequently, the UV light source was turned on to formally start the photocatalytic degradation process. During the reaction process, samples were taken from the same location at set time points. The water samples taken were quenched with $Na_2S_2O_3$ and then filtered through a 0.22 μm filter membrane. The filtrate samples were analyzed by high performance liquid chromatography (HPLC).

The study investigated the effects of N,Fe-CDs/PMS concentration, solution pH, temperature and co-existing pollutants/substances on the oxidizing performance (as indexed by CBZ removal).The CBZ removal efficiency (η, 100%) was calculated according to the following equation (1).

$$\eta = \frac{C_0 - C}{C_0} \times 100\% \quad ((1)$$

Where η is the degradation rate, %; C_0 is the initial concentration of CBZ, mg/L; C is the concentration of CBZ at t min, mg/L. The degradation rate of CBZ at t min was 0.5 mg/L and the degradation rate of CBZ at t min was 0.5 mg/L.

2.4. Methods of analysis

The concentration of pollutants was determined using a Shimadzu LC-20A high-performance liquid chromatography (HPLC) system. The mobile phase consisted of HPLC-grade acetonitrile (Phase A) and ultrapure water (Phase B) in a volume ratio of 55:45. The flow rate was set at 1.0 mL/min, the column temperature was maintained at 30°C, and the injection volume was 10 μL. Detection was carried out at a wavelength of 270 nm using an ultraviolet detector. Under these conditions, the retention time of CBZ was observed to be 5.2 mins.

Fe(II) concentration was measured according to the Chinese national standard “Water Quality – Determination of Iron – o-Phenanthroline Spectrophotometric Method (for Trial Use)” (HJ/T 345-2007), which was employed to monitor the Fe(II) concentration and its dynamic changes during the reaction (see Text S1 for details). Degradation intermediates of CBZ were detected using HPLC-MS/MS, while Gaussian 16 quantum chemical calculation software was used for structure optimization and reactivity analysis of the CBZ molecules (for detailed methodology, refer to Text S2).

2.5. Toxicity measurements

The toxicity of carbamazepine (CBZ) and its degradation intermediates was assessed using the T.E.S.T ecotoxicity prediction software, which operates on the principle of quantitative structure-activity relationship (QSAR) modeling. The software allows quick assessment of the possible toxicity of compounds through entering their 2 or 3D molecular structures and run a variety of models of algorithmic approaches. The acute toxicity to Daphnia magna, an aquatic invertebrate, was evaluated using T.E.S.T software, with structural characterization of each

intermediate. The primary endpoint of the analysis was the 48-hour median lethal concentration (LC_{50}). Additionally, environmentally relevant toxicity parameters, including developmental toxicity, mutagenicity, and bioconcentration factor (BCF), were predicted and analyzed.

3. Results and discussion

3.1. Characterization of N,Fe-CDs

3.1.1. The appearance of N,Fe-CDs

Figure S1 shows that N,Fe-CDs particles exhibit uniform distribution and near-spherical morphology, demonstrating excellent dispersion with no visible agglomeration. High-resolution images reveal lattice fringes with an interplanar spacing of approximately 0.22 nm (**Figure S1c**), consistent with the (100) plane of graphitic carbon. Statistical analysis based on 100 particles (**Figure S1d**) indicates that the average particle size of N,Fe-CDs is 4.58 ± 0.08 nm, with a particle size distribution following an approximate Gaussian distribution, primarily concentrated in the 3.25–6.25 nm range.

3.1.2. The crystal structure of N,Fe-CDs

The XRD pattern of N,Fe-CDs was shown in **Figure 1a**. A sharp diffraction peak at 19.25° indicated that Fe in N,Fe-CDs primarily existed in an amorphous state rather than forming iron oxide crystals(Li, Q.S. *et al.* 2022). The diffraction peak at 23.61° in N-CDs was close to the (002) crystallographic plane of graphitic carbon, which was similar to the N-doped CDs prepared by Zhang *et al.* (Zhang *et al.* 2016) using ammonia as a nitrogen source. Compared to the graphitic carbon peak in N-CDs, the carbon peak of N,Fe-CDs was slightly shifted to 23.1°, suggesting that they still maintained an amorphous structure and underwent lattice contraction. This change was possibly linked to the active sites generated in N,Fe-CDs(Mir *et al.* 2023). Moreover, the amount of the graphite peaks within N,Fe-CDs was significantly less than the amount within the N-CDs hence the implication that Fe has been effectively doped in the sp^2 graphite framework(Li *et al.* 2018).

3.1.3. Surface chemistry and photoelectronic properties

peaks observed at 3430 cm^{-1}, 3160 cm^{-1}, 3006 cm^{-1}, 1405 cm^{-1}, 1720 cm^{-1}, and 1203 cm^{-1}, corresponding to the stretching vibrations of -OH, N-H, C-H, C=N, C=O, and C-O, respectively (Al-Qahtani *et al.*, 2022). These findings proved the effective doping of nitrogen of the graphitic carbon structur (Ahmadian-Fard-Fini *et al.* 2021). Furthermore, as shown in **Figure 1d**, compared to N-CDs, the N,Fe-CDs exhibited transmission peaks of Fe-OH, Fe-O, and Fe-N in the lower wavelength region (1000–500 cm^{-1}), with Fe-O dominating at 845 cm^{-1}, 600 cm^{-1}, and 540 cm^{-1}, respectively. The resulting findings showed that doping or coordination of the iron into the carbon dots is successful (Jiang *et al.* 2025). The above observations also indicated that N, Fe-CDs had an added signal due to the presence of functional groups (H2O and CO) surface, which was at 710 eV with respect to N-CDs, which was the Fe 2p peak and indicated that Fe had been successfully doped onto the N,Fe-CDs. The O 1s and Fe 2p signals of N,Fe-CDs were much stronger than the signals of N-CDs, which indicated that the introduction of Fe could stimulate the appearance of the oxygen functional groups on the surface of the material, including this hydroxyl, carboxyl, or iron oxide species. The increase in activity and distribution of reactive sites on the surface was probably increased by this enhancement. Moreover, N,Fe-CDs and N-CDs had distinct peaks at about 284 e V, 532 e V, and 400 e V, respectively, and which were attributed to C, O, and N respectively. This was a sign that nitrogen had been successfully doped in the materials and as per the peak intensity, C, N and O were identified as the primary constituent of the carbon dots.

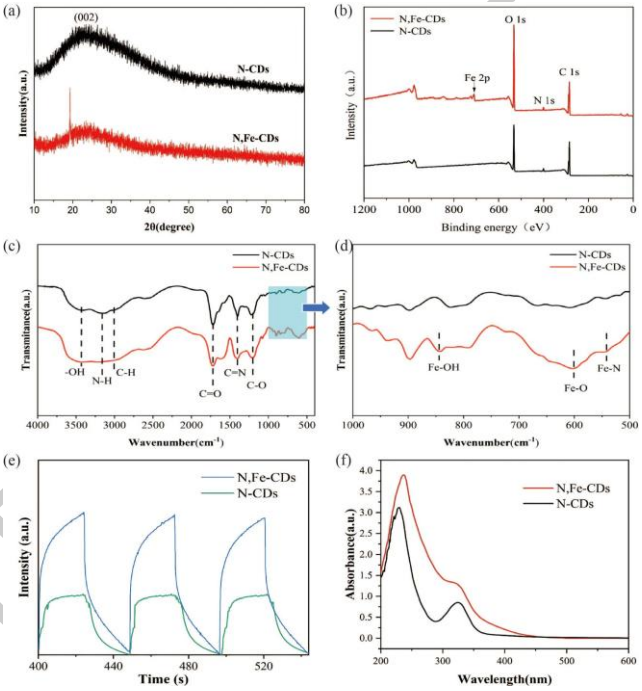

Figure 1. (a) XRD patterns; (b) XPS Scanning Spectra; (c-d) The FTIR images; (e) Transient photocurrent response spectrum; (f) UV-Vis Absorption Spectra;

Figure 1f showed that N,Fe-CDs had great absorption characteristics at the ultraviolet (UV) selection. The two absorption peaks found at 240 nm and 320 nm were reported to belong to the sp^2 to graphite carbon and n p + transitions of C=O and C=N, respectively. The n- 0 - Fe -N coordination bonds formed a slight shift in the n - 0 - Fe -N absorption peak of N,Fe-CDs as compared to N-CDs (Chang *et al.* 2021). Furthermore, the doping of transition metal Fe resulted in the formation of Fe-O, Fe-N, and Fe-OH complexes, which enhanced the absorption of N,Fe-CDs in the UV-visible region, thereby broadening the absorption range of the carbon dots (Chang *et al.* 2021). As shown in **Figure 1e**, transient photocurrent response experiments indicated that the photocurrent intensity of N,Fe-CDs significantly increased over multiple light-switching cycles. Compared to N-CDs, N,Fe-CDs exhibited a higher photocurrent response, suggesting that N,Fe-CDs were more efficient in separating and transferring photogenerated electrons (Jiang *et al.* 2025).

3.2. Effectiveness of UV/N,Fe-CDs/PMS systems

3.2.1. Comparison of degradation effect of CBZ under different systems

To reveal the synergistic mechanism of multi-systems, the degradation ability of different reaction systems for CBZ under the same conditions was compared. As shown in **Figure 2a**, the system reached adsorption-desorption equilibrium after 30 mins in the dark, and the degradation reaction did not proceed significantly. In the blank UV, N-CDs, N,Fe-CDs single system, the degradation efficiency was extremely low with $C/C_o > 0.85$ due to the lack of oxidant or photocatalytic activation. After the introduction of PMS, the UV/PMS system directly activated PMS by UV light to produce $SO_4\bullet^-$ and •OH, and the degradation rate was increased to 46.1%, but was limited by the activation rate; in the UV/Fe^{3+}/PMS system, Fe^{3+} promoted the transfer of electrons under UV irradiation, and was reduced to Fe^{2+}(Ling *et al.* 2017), which improved the degradation efficiency. The activation efficiency was improved, and the degradation rate reached 53.7%, but it still did not break through the limitation of traditional iron-based catalysts; the UV/N-CDs/PMS system took advantage of the electron acceptor property of N-CDs to enhance the generation of ROS through interfacial reaction, and the C/C_o was reduced to 0.52, and the degradation rate was about 48%, which demonstrated the ability of nitrogen-doped carbon dots in the activation of PMS; the UV/N,Fe-CDs/PMS system was also improved by the UV irradiation. The UV/ N,Fe-CDs/PMS system showed the best performance, with the degradation rate of CBZ reaching 95.4% in 20 mins, which was much higher than that of the other systems. The high efficiency of the UV/N,Fe-CDs/PMS system was attributed to the fact that the Fe-O/N/OH bonds in the N,Fe-CDs enhanced the stability of iron ions and accelerated the electron transfer, which significantly enhanced the activation efficiency of the PMS, and thus increased the yields of $SO_4\bullet^-$ and •OH. **Table 1** shows a comparison with other treatments demonstrating the high efficiency of the UV/N,Fe-CDs/PMS degradation system.

Table 1. Degradation efficiency of CBZ by UV/N,Fe-CD/PMS with other treatments

Catalyzer	Experimental condition	CBZ concentration	Degradation time/efficiency	Reference
Fe-Cu binary oxide	[Fe-Cu binary oxide] = 1.5 g/L; [H_2O_2] = 0.2 M	2 mg/L	180 min/100%	(Zhu *et al.* 2022)
Fe^0	[Fe^0] = 0.4 g/L; [H_2O_2] = 100 mM ultrasound	10 mg/L	30 min/95%	(Ghauch *et al.* 2011)
Cl	[Cl] = 600 μM UV	5 mg/L	70 min/88.6%	(Yang *et al.* 2016)
Fe^{2+}	[Fe^{2+}] = 17.91 uM; [H_2O_2] =1.06 mMultrasound	5 mg/L	600 min/90.6%	(Wang and Zhou 2016)
Fe^0	[Fe^0] = 0.4 g/L; [PDS] = 0.4 mg/L ultrasound	5 mg/L	60 min/98.4%	(Ali *et al.* 2018)
N,Fe-CDs	[N,Fe-CDs] = 0.1 g/L; [PMS] = 0.5mM 10W UV	10 mg/L	20 min/95.4%	This study

3.2.2. Effect of N,Fe-CDs/PMS concentration

The effect of different PMS concentration (0.1-0.7 mM) systems on the degradation of CBZ was experimentally investigated and the results are shown in **Figure 2c**. When the PMS concentration was increased from 0.1 mM to 0.7 mM, the degradation rate of CBZ increased from 41% to 96.7% after 20 mins of reaction, and the value of k, the degradation rate constant, was gradually increased from 0.021 min^{-1} (0.1 mM) to 0.161 min^{-1} (0.7 mM). However, the increase gradually leveled off between 0.5 mM and 0.7 mM.

Different concentrations (0.06-0.12 g/L) of N,Fe-CDs were also set up to investigate their effects on the degradation efficiency of CBZ, and the results are shown in **Figure 2b**. The degradation rate and degradation efficiency of CBZ increased significantly with the gradual increase of N,Fe-CDs concentration. When the dosage of N,Fe-CDs was increased from 0.06 g/L to 0.12 g/L, the degradation rate of CBZ increased from 67.4% to 96.9% after 20 min reaction, but the degradation effect of 0.12 g/L was not much different from that of 0.10 g/L condition. This trend is also shown by the change of k value in **Figure 2b**, which increased from 0.101 min^{-1} to 0.144 min^{-1} as the concentration increased from 0.06 g/L to 0.10 g/L, and further increased to 0.170 mins at 0.12 g/L catalyst dosage. Above 0.10 g/L, the high concentration of catalyst may lead to the excessive generation of free radicals, which triggers the self-bursting reaction between the free radicals, thus leading to a slowing down of the increase in the CBZ degradation rate (Fan *et al.* 2018). Therefore, considering the cost and high activity, subsequent experiments were conducted using 0.5 mM PMS and 0.10 g/L N,Fe-CDs.

3.2.3. Effect of Temperature

The impact of temperature on CBZ degradation was assessed in the range of 25°C to 55°C. As shown in **Figure 2d**, the degradation rate of CBZ increased from 95.4% to 99.1% as the temperature rose, and the degradation process was significantly accelerated. The rate constant (k-value) progressively increased from 0.144 min^{-1} to 0.222 min^{-1}. However, at 55°C, the k-value slightly decreased to 0.201 min^{-1}, indicating a positive influence of temperature on the reaction kinetics up to a point. The elevated temperature enhanced the degradation performance through two primary mechanisms: firstly, the high temperature accelerated the surface activation of PMS by the catalyst, increasing the generation rate of free radicals like $SO_4\bullet^-$ and •OH (Liu *et al.* 2021); secondly, the increased temperature boosted the frequency and energy of collisions between free radicals and pollutants (Yentür and Dükkanci 2020). The slight decrease in the k-value at 55°C compared to 45°C can be attributed to the fact that excessively high temperatures may accelerate the self-

decomposition or side reactions of PMS, thereby reducing the yield of effective radicals.

3.2.4. Effect of pH

The degradation behavior of CBZ was also systematically studied across different pH values. As illustrated in **Figure 2e**, the system exhibited good degradation performance under acidic conditions (pH = 3 and pH = 4). However, as the pH increased to 5, 7, and 9, the degradation efficiency of CBZ gradually declined from 94.8% to 72.1%, 74.1%, and 78.5% within 20 mins. When the pH was greater than 3, Fe^{3+} tended to form $Fe(OH)_3$ precipitation (Zhang *et al.* 2019; Zhao *et al.* 2021), which hindered the activation of PMS. However, the N,Fe-CDs were successful in stabilizing the Fe ions through chelation with a similar degradation rate when the pH = 4 (k = 0.143 min^{-1}) to that when the pH = 3 (k = 0.139 min^{-1}). This showed that the system was better stable when in a weakly acidic medium (pH 3-4). At pH 5-9 (k = 0.064-0.074 min -1), the degradation rate became much lower. Despite the reduced efficiency in neutral and alkaline conditions, the system retained some degradation capability over a wide pH range (3-9). This suggests that the chelation between the functional groups in N,Fe-CDs and Fe^{3+} significantly improved the stability of Fe^{3+}, highlighting that the UV/N,Fe-CDs/PMS system possesses a certain degree of pH adaptability.

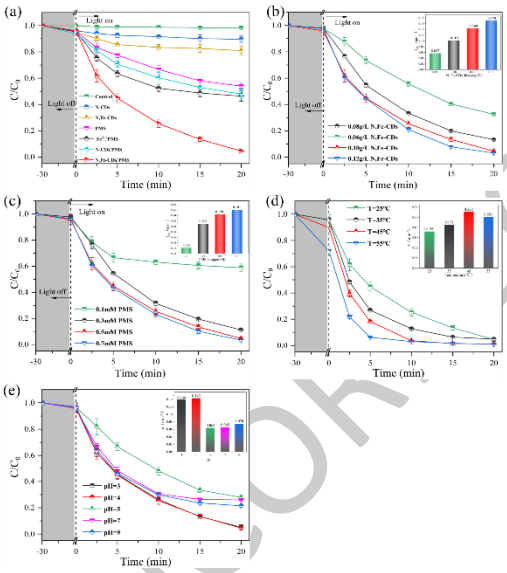

Figure 2 (a) Effect of different reaction systems;(b) Effect of PMS dosage;(c) Effect of N,Fe-CDs dosage;(d) Effect of pH;(e) Effect of temperature;Experimental conditions:CBZ = 10 mg·L^{-1}, PMS = 0.5 mM, catalyst dosage = 0.1 g·L^{-1}, temperature =25℃, The initial pH of all reactions is not adjusted, stirring speed =300 r/m

3.2.5. Effects of coexisting substances

To investigate the effects of multiple coexisting substances in natural water, experiments were conducted to evaluate the impact of various cations (e.g., Mg^{2+}, NH_4^+), anions (e.g., Cl^-, NO_3^-, SO_4^{2-}, HCO_3^-), and humic acid (HA) on the degradation of CBZ using the UV/N,Fe-CDs/PMS system. As shown in **Figure 4a**, the reaction was divided into two phases: a dark reaction phase (-30 mins to 0 mins) and a UV illumination phase (0 mins to 20 mins). Throughout the reaction, Cl^- and HCO_3^- exhibited significant inhibitory effects on CBZ degradation. When the concentration of Cl^- reached 15 mM, the degradation rate of CBZ was significantly slowed, demonstrating a strong inhibitory effect (**Figure 3a**). The degradation efficiency leveled in the concentration of HCO_3^- of 5, 10 and 15 mM and the end values of C/C_0 kept constant in the range of 0.65 to 0.70. It shows that the degradation process was concentration-dependently inhibited by both Cl^- and HCO_3^-, meaning that their interactions with reactive free radicals like 0H and SO_4^{2-} result in the formation of less reactive radicals and, accordingly, reduced the efficiency of the degradation process (**Figure 3b**).The inhibitory activity of Cl^- and HCO_3^- could be explained by the fact that they acted on reactive free radicals and, thus, formed less reactive radicals and, consequently, decreased the efficiency of the degradation process Minimal effects could be detected on CBZ degradation by NO_3^- within the 5-15 mM concentration range (**Figure 3c**). SO_4^{2-} - in the presence of 5 mM and 10 mM concentration was useful in CBZ-decomposition under UV light. But, at higher concentration of SO_4^{2-} - of 15 mM, the rate of degradation was slow, and the photoresponsive degradation rate was consistently lower than other groups, but it has clearly shown that there is an inhibitory effect (**Figure 3d**). The concentration of SO_4^{2-}- (5-10 mM) stimulated the degradation of CBZ, which stimulated the production of the SO_4^{2-} radicals, which in turn increased the degradation rate (Huie *et al.* 1988; Jiang *et al.* 2025). Conversely, the degradation rate decreased as depicted in the presence of higher ionic strength (15 mM) that prevented the diffusion of free radicals.

$$HCO_3^- + \bullet OH \rightarrow CO_3\bullet^- + H_2O \quad (E^o=1.5\ V) \qquad (2)$$

The C/C_0 value was lower in the dark reaction stage with an increase in the concentration of Mg^{2+}. In this case, especially a C/C_0 value decreased to 0.6 at the condition of 15 mM Mg^{2+} +. It can be credited to the fact that Mg^{2+} + compresses the electric layer on the surface of N,Fe-CDs in the solution, thereby decreasing the electrostatic repulsion and, consequently, increasing the number of pollutant molecules attached to N,Fe-CDs and PMS. The rate of degradation of the system was greatly decreased during the step of photoreaction. The degradation rates in 0, 5, 10 and 15 mM Mg^{2+} - were observed to be lower than 80 percent in 20 mins and the reaction curves were evened after 10 mins (**Figure 3e**). The effect is reflected in the result of Wu *et al.* (Wu *et al.* 2021). Mg 2+ has been reported to raise the activation energy of majority of the direct photolysis pathways of pollutants (Wang and Wang 2017); thereby suppressing the rate of reaction. NH_4^+ also demonstrates a similar dual effect (**Figure 3f**): by increasing ionic strength, it reduces electrostatic repulsion between N,Fe-CDs and the pollutants, promoting the adsorption and enrichment of pollutants on the catalyst surface. However, during the photoreaction phase, NH_4^+ undergoes chain quenching reactions with $SO_4\bullet^-$ and •OH, generating amino radicals ($NH_2\bullet$, E^o = 1.0 V) with low oxidizing ability, which in turn weakens the overall oxidative degradation capacity of the system.

Under UV irradiation, the substantial generation of ROS allowed the system's degradation rate to reach 93.4% in the presence of 5 mg/L HA, with only a 2% decrease; the

degradation rate remained higher than that of the group without HA over a period of time (**Figure 3g**). This indicates that HA, acting as a photosensitizer under UV, generates a significant amount of reactive substances such as triplet chromophores DOM, hydroxyl radicals, and singlet oxygen, which enhances the removal of water pollutants (Santoke *et al.* 2012). Nonetheless, the degradation efficiency of the system started to decrease with the increase of the HA concentration up to 10mg/L and the inhibition became stronger with the further increase of the HA concentration, up to 20mg/L. This phenomenon is closely related to the shading effect and free radical quenching effect of HA (Chen *et al.* 2013; Kang *et al.* 2018), leading to a reduction in the removal of target pollutants. Additionally, HA can form complexes with metal ions such as Fe^{2+}, which affects the activation reaction between N,Fe-CDs and PMS.

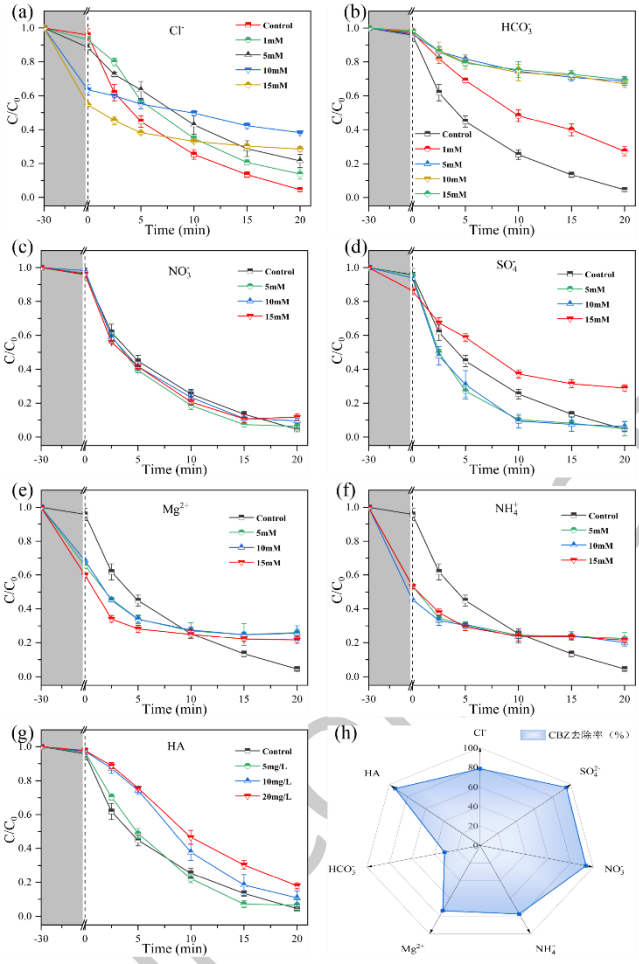

Figure 3. (a) Effects of different concentrations of Cl^- ;(b) Effects of different concentrations of HCO_3^-;(c) Effects of different concentrations of NO_3^-;(d) Effects of different concentrations of SO_4^{2-};(e) Effects of different concentrations of Mg^{2+};(f) Effects of different concentrations of NH_4^+;(g) Effects of different concentrations of HA;(h) UV/N,Fe-CDs/PMS Anti-Ion Interference Radar Map ;Experimental conditions:CBZ = 10 mg·L^{-1}, PMS = 0.5 mM, catalyst dosage = 0.1 g·L^{-1}, temperature =25℃, The initial pH of all reactions is not adjusted, stirring speed = 300 r/m

Combining the effects of coexisting ions and organic matter, **Figure 3h** presents the radar plot of CBZ removal by the UV/N,Fe-CDs/PMS system under different coexisting ion conditions. The results show that Cl^-, SO_4^{2-}, NO_3^-, and HA had little effect on degradation, maintaining a high removal rate above 80%. Mg^{2+} and NH_4^+ caused slight interference, but overall, the effect was weak, while HCO_3^- significantly inhibited CBZ removal.

3.3. Mechanism of CBZ removal by UV/N,Fe-CDs/PMS system

3.3.1. Identification of reactive species

To investigate the mechanism of CBZ degradation in the UV/N,Fe-CDs/PMS system, it is essential to understand the primary ROS involved in the degradation process. The possible ROS include $SO_4\bullet^-$, •OH, $^1O_2$, and $\bullet O_2^-$. It is well-established that TBA reacts rapidly with •OH but is not efficiently oxidized by -$SO_4\bullet^-$(Liang and Su 2009). Consequently, TBA was introduced as a scavenger for •OH in the experiments to assess its contribution to CBZ removal. As shown in **Figure 4a**, the final CBZ degradation decreased from 95.3% to 85.2% when the TBA concentration was increased from 50 mM to 500 mM, indicating that •OH plays a minor role in CBZ removal and is not the primary active oxidant.MeOH has fast reaction kinetics with -$SO_4\bullet^-$ and •OH, which effectively arrests both involvements of radicals in equilibrium and with low efficiency (Liu, N. *et al.* 2021). The rate of the degradation of CBZ did not change significantly with the increased concentration of MeOH (0 to 50 mM). Yet, the degradation rate of CBZ was reduced dramatically with a further increase in the MeOH concentration to 5 M (**Figure 4b**), which indicates that the $^1O_2$ and $\bullet O_2^-$ existed in the UV/N,Fe-CDs/PMS system, as well as the quenching effect of high MeOH concentration, significantly inhibited the degradation capacity of the system.Increased p-BQ and FFA were used to investigate the roles of $^1O_2$ and $\bullet O_2^-$ in the system. These findings, represented in **Figure 4c-d**, suggest that the action of p-BQ and FFA was an effective inhibitor of CBZ degradation. In the concentration of 1 mM adopting p-BQ and FFA, the rate of degradation decreased to 15.4 and 11 percent, respectively, with minimal additional decrease in the concentration. According to the findings of the sample of free radical and non-radical quenching experiments, the concentration of four ROS in the system was verified. The non-radical $^1O_2$ and the radical $\bullet O_2^-$ were found to be the most important active species and -$SO_4\bullet^-$ and •OH were the secondary active species. Additionally, there may be a synergistic interaction between the ROS.

In situ EPR spin-trapping confirmed ROS generation in the UV/N,Fe-CDs/PMS system.The EPR spectra are shown in **Figure 4(a-c)**, which share identical axes.In **Figure 4a**, DMPO (25 mM) was used to trap radicals.The spectrum shows the characteristic 1:2:2:1 quartet of DMPO-•OH, with a shoulder signal attributable to DMPO-$SO_4\bullet^-$.These signals indicate the coexistence of •OH and $SO_4\bullet^-$ under UV irradiation.The DMPO-•OH signal was stronger than DMPO-$SO_4\bullet^-$, suggesting higher •OH formation, potentially because $SO_4\bullet^-$ contributes to •OH generation.In **Figure 4b**, DMPO captured $\bullet O_2^-$, yielding a clear signal with an intensity ratio of 2:2:1:2:1:2.In **Figure 4c**, TEMP (25 mM) trapped $^1O_2$, producing the typical 1:1:1 triplet with a markedly higher intensity than the radical signals.This confirms the presence of $^1O_2$ and suggests that it is the

dominant ROS in the UV/N,Fe-CDs/PMS system.No corresponding EPR signals were detected in the dark.Therefore, ROS generation is UV-dependent, and UV irradiation serves as the key driving force for reactive species formation.

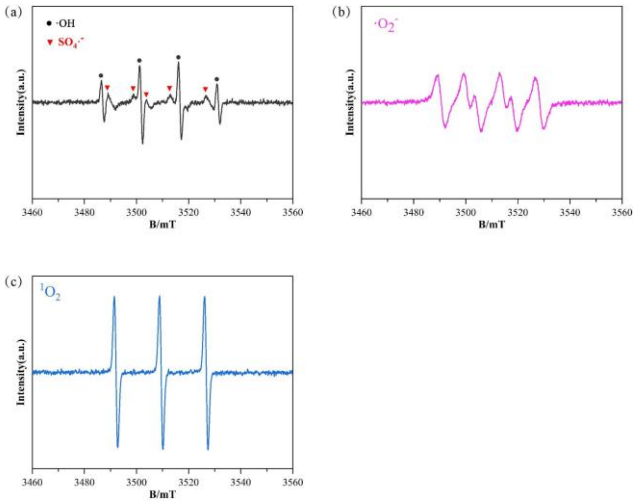

Figure 4. EPR spectra: (a) DMPO-•OH,DMPO-SO_4•$^-$; (b) DMPO-•O_2^-; (c) TEMP-$^1O_2$

3.3.2. Conversion of iron ions

In the transition metal-catalyzed PMS advanced oxidation system, the introduction of iron significantly accelerated the free radical generation rate during PMS activation, a process that likely expedited the Fe^{3+}/Fe^{2+} redox cycle. To investigate this, researchers monitored the formation of iron ions under both dark and UV light conditions. Under UV irradiation, Fe^{3+} in N,Fe-CDs can be effectively reduced to Fe^{2+} by the photogenerated electrons (e^-) in the graphene structure within the carbon dots, showing a clear accumulation of photogenerated Fe^{2+} (**Figure 5e**). This suggests that N,Fe-CDs can facilitate the reduction of Fe^{3+} to Fe^{2+} during a 20-mins degradation reaction. Upon the addition of PMS, the concentration of photogenerated Fe^{2+} in the system significantly decreased compared to the system without PMS. This reduction is likely due to the reaction of Fe^{2+} with PMS, leading to the formation of sulfate radicals (SO_4•$^-$).

3.3.3. Activation mechanism analysis

Based on the identification of system ROS and the analysis of the results of iron ion conversion, a mechanism for the catalytic degradation of the UV/PMS system enhanced by N,Fe-CDs was proposed, as shown in **Figure 6**. Previous studies have shown that the UV/PMS system mainly generates •OH and SO_4•$^-$ (Eq. 3), and these two radicals were also detected in the UV/N,Fe-CDs/PMS system. Under UV irradiation, the sp^2 graphitic carbon structure of N,Fe-CDs absorbs photon energy, leading to electronic transitions that generate photogenerated electrons (e^-). Through a ligand-to-metal charge transfer (LMCT) process, Fe^{3+} acquires electrons from O, N, or OH ligands and is rapidly reduced to Fe^{2+} (Eq. 5). The Fe^{2+} generated by reduction plays a central role in driving and enhancing the degradation reaction. Fe^{2+} reacts with PMS to generate strong oxidizing radicals such as SO_4•$^-$ and •OH, while Fe^{2+} is oxidized back to Fe^{3+} (Eq. 6). SO_4•$^-$ can further react with H_2O to form •OH (Eq. 4)(Zhao *et al.* 2021). Under UV irradiation, the interaction of Fe^{3+} with PMS promotes the generation of Fe^{2+} (Eq. 7)(Ling *et al.* 2017). Simultaneously, the photogenerated electrons in N,Fe-CDs can convert dissolved oxygen into •O_2^- (Eq. 11). Fe^{2+} in the system can be oxidized to Fe^{3+} by dissolved oxygen and react with it to form •O_2^- (Eq. 12)(Song, H. *et al.* 2015; Yang *et al.* 2016). Research has shown that Fe^{2+} may be further converted to high-valent Fe(IV) in the presence of PMS (Jiang *et al.* 2025). Although this intermediate has a short lifetime, it exhibits high reactivity in degrading pollutants, ultimately decaying back to Fe^{3+} or Fe^{2+}(Tian *et al.* 2023). Therefore, high-valent Fe (IV) may also exist in the system, warranting further exploration.

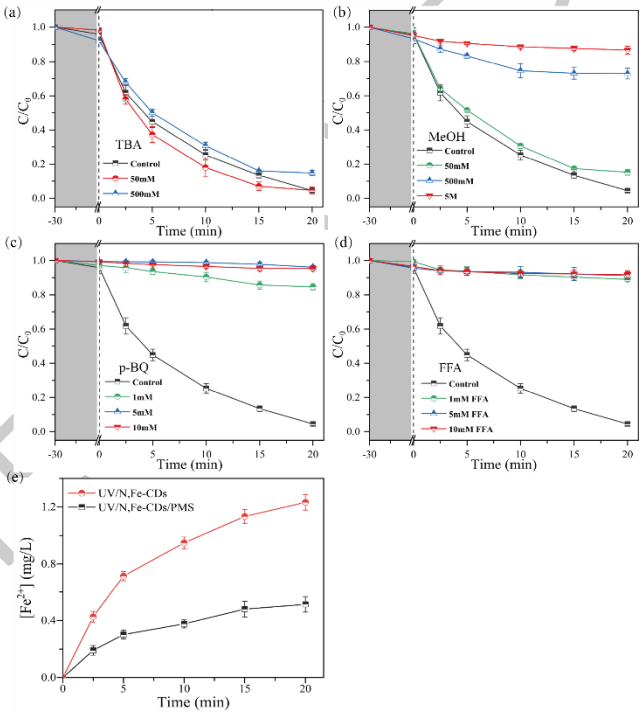

Figure 5. (a) Effect of TBA;(b) Effect of p-BQ;(c) Effect of MeOH;(d) Effect of FFA;(e) Photogenerated Fe^{2+} production in different systems; Experimental conditions: CBZ = 10 mg·L^{-1}, PMS = 0.5 mM, catalyst dosage = 0.1 g·L^{-1}, temperature =25℃, The initial pH of all reactions is not adjusted, stirring speed = 300 r/m

Based on the involvement of reactive oxygen species (ROS) and the observed Fe redox transformations, a catalytic degradation mechanism for the UV/N,Fe-CDs/PMS system is proposed (**Figure 6**). Past experimental results have shown that the main products of the UV/PMS system are hydroxyl radicals (•OH) and sulfate radicals (SO_4•$^-$) (Eq. 3) both of which were also observed in UV/N,Fe-CDs/PMS system. The sp^2 graphitic carbon structure of N,Fe-CDs absorbs the UV irradiation photon energy leading to electronic transitions that produce photogenerated electrons (e^-). Fe^{3+} generates electrons on O, N, or OH ligands by a ligand-to-metal charge transfer (LMCT) mechanism and is then promptly reduced to Fe^{2+} (Equation 5). The Fe^{2+} produced in this reduction become the key ingredient in catalyzing and boosting the degradation reaction. Fe^{2+} and PMS react to generate good oxidizing radicals like SO_4•$^-$ and •OH, whilst Fe^{2+} is oxidized to Fe^{3+} (Equation 6). SO_4•$^-$ may also react with H_2O to produce

•OH (Equation 4)(Zhao, G.Q. *et al.* 2021).Fe^{3+} + reacts with PMS under UV irradiation to facilitate the formation of Fe^{2+} (Eq. 7)(Ling *et al.* 2017). Meanwhile, photoexcited electrons from N,Fe-CDs can reduce dissolved O_2 to $•O_2^-$ (Eq. 11). Fe^{2+} can also react with dissolved O_2 to form Fe^{3+} (Eq. 12), which may subsequently react with $•O_2^-$(Song, Hui *et al.* 2015). It has been shown that Fe^{2+} can be further oxidized to Fe (IV) high-valence form by PMS(Ahmadian-Fard-Fini *et al.* 2021). Though the lifetime of this intermediate is low, it is highly active in decomposing pollutants and eventually breaks down to Fe^{3+} or Fe^{2+} (Liang and Su 2009). Therefore, the potential involvement of high-valent Fe(IV) warrants further investigation.

Besides the abovementioned free radical pathways, the non-radical pathway degrades CBZ mainly by $^1O_2$, that contributes a major share to the degradation process. Primary routes to $^1O_2$ production are the product of PMS with Fe^{3+} to yield $•SO_5^-$ - under UV radiation, where the product can be formed by self-reaction or reacting with water (Eqs. 8 and 9); alternatively, it can be formed by self-decomposition of PMS (Eq. 10)(Li, X. *et al.* 2022); or by reduction of the product with water (Eq. 13) (Shahzad *et al.* 2019). Overall, the UV/N,Fe-CDs/PMS system provides multiple pathways for the oxidative attack of CBZ molecules. Among these, $•O_2^-$ and $^1O_2$ are the primary key oxidizing agents in the degradation system. While •OH and $SO_4•^-$ also possess strong oxidative abilities, in this system, they act more as synergistic contributors, further increasing the overall degradation rate.

$$HSO_5^- \xrightarrow{UV} •OH + SO_4^{2-} + H^+ \quad (3)$$

$$Fe^{3+} + e^- \rightarrow Fe^{2+} \quad (4)$$

$$Fe^{2+} + HSO_5^- \rightarrow Fe^{3+} + SO_4^{•-} \quad (5)$$

$$Fe^{3+} + HSO_5^- \xrightarrow{UV} Fe^{2+} + •SO_5^- + H^+ \quad (6)$$

$$2•SO_5^- \rightarrow 2SO_4^- + {}^1O_2 \quad (7)$$

$$•SO_5^- + H_2O \rightarrow HSO_5^- + {}^1O_2 \quad (8)$$

$$HSO_5^- + SO_5^{2-} \rightarrow SO_4^{2-} + HSO_4^- + {}^1O_2 \quad (9)$$

$$O_2 + e^- \rightarrow •O_2^- \quad (10)$$

$$Fe^{2+} + O_2 \rightarrow Fe^{3+} + •O_2^- \quad (11)$$

$$2•O_2^- + 2H_2O \rightarrow {}^1O_2 + H_2O_2 + 2OH^- \quad (12)$$

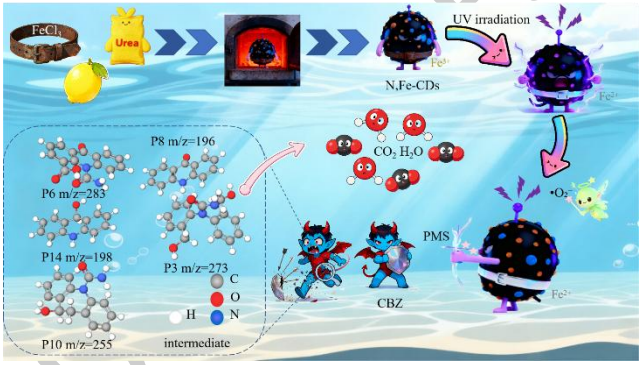

Figure 6. Degradation system activation mechanism diagram

3.3.4. Degradation product pathway

The preliminary construction of the 3D molecular structure of the target pollutant carbamazepine (CBZ) was carried out using GaussView 6 software, and the molecular structure was geometrically optimized using density-functional theory (DFT) on the Gaussian 09W platform. The specific calculation parameters are shown in **Table 2.**

Table 2. Optimized computational parameters for CBZ

Name	Calculation type	calculation method	base group	rotation scheme	background solvent
Parameter	FREQ	B3LYP	6-31g(d,p)	one-line state	H_2O

The optimized electrostatic potential (ESP) map of carbamazepine (CBZ) (**Figure 7a**) reveals a dipole moment of 5.187 D, confirming its strongly polar nature. Notably, the central seven-membered N-heterocycle exhibits the most negative ESP values (deepest red regions), indicating high local electron density and pronounced electron-donating character. This electronic feature correlates with elevated chemical reactivity and reduced structural stability in the heterocyclic region, making it preferentially susceptible to attack by reactive oxygen species (ROS). Consequently, the C–N, C–C, and C=C bonds within this ring are predicted as primary cleavage sites during oxidative degradation.

This insight into mechanism can be further shown by DFT analysis of frontier molecular orbitals (**Figure 7b-c**). The Highest Occupied Molecular orbital (HOMO) is found to exhibit a high concentration of electron density on the N-heterocycle, mainly around the atom at position N23 (**Figure 7b**, blue/green lobes). These electron-rich areas expose nucleophilic reaction or oxidation by electrophilic radical species. On the other hand, the Lowest Unoccupied Molecular Orbital (LUMO) remains electron-deficient (**Figure7c**, brown lobes) at the benzene rings (mainly), which imply electron attacks. These orbital distributions patterns are consistent with the known hydroxylation initiated ring opening at the heterocycle during degradation.

HPLC-MS/MS was used to identify 14 major intermediates that were generated in the process of degradation that were identified as P1-P14 (**Table S2**) to further study the mechanism of degradation of CBZ in the UV/N,Fe-CDs/PMS system. According to these data, the suggested

degradation pathway of CBZ included in **Figure 8** oxidation, hydroxylation, epoxidation and the cleavage of bonds. The seven-membered azepine ring and adjacent aromatic rings represent preferential sites for radical attack due to their high electron density (Bu *et al.* 2018). In these areas, epoxidation and hydroxylation yield oxygenated intermediates P1 and P2(Zhang *et al.* 2023). These results are consistent with the DFT analysis and also, they verify the important role of hydroxyl radicals (-OH) in CBZ degradation. This finding is consistent with the DFT results and confirms the vigorous electrophilicity of -OH on the CBZ molecules. During further oxidation reactions, a portion of the P2 was changed into the dihydroxy product P3(Ding *et al.* 2017) and dehydrogenation product P4. The OH group of P4 was further oxidized to carbonyl group and this produced the amide structure P5, which serves as a common intermediate in the CBZ degradation processes by breaking it down through advanced oxidation processes (AOPs). P5 was oxidized into P6 by the catalysis of ROS in the later oxidation processes, and the carbonyl group was splintered to produce the aldehydes and ketones of low molecular weight (P7 and P8) (Liu *et al.* 2020). P3, in the meantime, was oxidized to P9 with help of ring-opening and then, by dehydroxylation and deamidation, into P12, comprising of an acridinone backbone. The aza-structure of P12 was further rearranged and decarboxylated under strong oxidative conditions to form P13, a lower-molecular-weight compound. Ultimately, P13 was oxidized by singlet oxygen ($^1O_2$) to form P14(Ding *et al.* 2017). All these intermediates are eventually mineralized into harmless small molecules, such as CO_2 and H_2O, under ROS-induced deep mineralization, leading to the complete removal of pollutants.

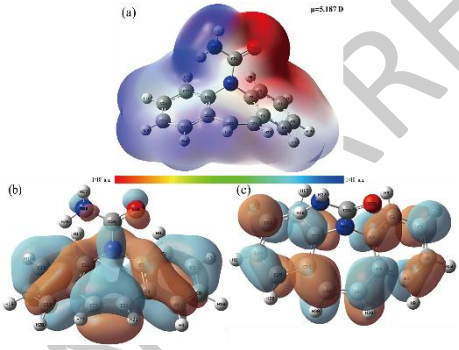

Figure 7. (a) molecular electrostatic potential diagram;(b-c) Orbital potential difference diagram;(b) HOMO;(c) LOMO

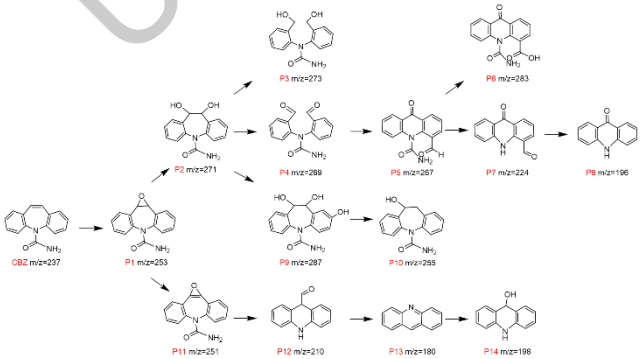

Figure 8. Possible degradation pathways of CBZ in UV/N,Fe-CDs/PMS systems

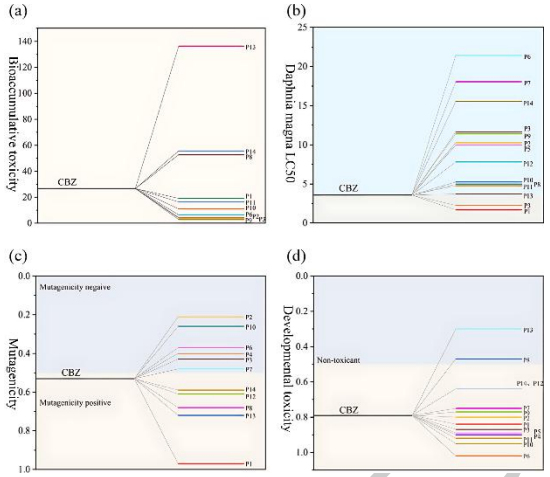

Figure9. (a) Bioaccumulative toxicity;(b) Daphnia magna LC50;(c) Mutagenicity;(d) Developmental toxicity

3.3.5. Toxicity assessment

To further evaluate the ecological safety of the UV/N,Fe-CDs/PMS system in the degradation of CBZ, the toxicity of CBZ and its main intermediates was predicted using T.E.S.T. software. The analyzed indexes included four aspects: bioconcentration factor (BCF), acute toxicity (LC50), mutagenicity, and growth and developmental toxicity in Daphnia magna. The results are shown in Figure 9. In Figure 9a, the BCF value of CBZ was 26.63, indicating a medium level of bioaccumulation. Most intermediates (e.g., P2, P3, and P10) showed lower BCF values than CBZ (<20), suggesting a reduced bioaccumulation risk. However, certain products such as P8 (52.7) and P13 (136.41) exhibited higher BCF values, warranting further attention to their ecological risks, which may be attributed to the increased presence of aromatic or carbonyl functional groups. In Fig. 9b, the 48-hour LC50 of CBZ for Daphnia magna was 3.56 mg/L, classifying it as “toxic.” After degradation, the LC50 values of most intermediate products significantly increased compared to CBZ. For instance, P6 (21.42 mg/L) and P7 (18.07 mg/L) exhibited low toxicity (>10 mg/L). Nevertheless, some intermediates remained acutely toxic, including P1 (1.69 mg/L) and P4 (2.26 mg/L). In Figure 9c, CBZ was predicted to be mutagenicity-positive, consistent with prior reports (Lu and Hu 2019). Among the degradation products, P8 (0.68) and P13 (0.72) maintained high mutagenicity, while intermediates such as P2 (0.21) and P10 (0.26) displayed mutagenic-negative or significantly reduced levels. Regarding developmental toxicity, Figure 9d demonstrates that the developmental toxicity index for CBZ was 0.79. The toxicity levels of intermediates P13 and P8 were significantly lower. In conclusion, the toxicity evaluation indicates that CBZ can be effectively degraded into less toxic products. However, some by-products still present certain risks in terms of BCF and mutagenicity, possibly due to the increased presence of aromatic or carbonyl functional groups.

4. Conclusion

In conclusion, this study rationally designed nitrogen–iron co-doped carbon dots (N,Fe-CDs) via a facile hydrothermal route as a low-iron, UV-responsive catalyst for PMS

activation. Characterization results show that the prepared N, Fe-CDs exhibit near-spherical nanostructures with good dispersion and typical graphitic carbon structure. Surface analysis confirms enrichment with hydroxyl, carbonyl, Fe-O, Fe-N, and Fe-OH bonds; these properties significantly enhance the UV-visible light absorption capacity and effectively promote photogenerated electron separation. Experimentally, the UV/N,Fe-CDs/PMS system achieved a 86.2% degradation efficiency for CBZ under optimal conditions within 20 min, representing a 2–5 fold enhancement over individual systems. This high degradation efficiency of 86.2% was maintained under a wide pH range (3-9) and high pollutant loading (30 mg/L). Cl^- and HCO_3^- anions exerted an inhibitory effect on the degradation system. Cations such as Mg^{2+} and NH_4^+ promoted the preliminary removal of CBZ during the dark reaction stage but exhibited a radical quenching effect under light conditions. Humic acid (HA) exhibited low-promotion and high-inhibition effect. The presence of four reactive oxygen species (ROS) in the UV/N, Fe-CDs/PMS system was also established by mechanistic studies: •OH, SO_4•$^-$, •O_2^-, and $^1O_2$. Among them, •OH, SO_4•$^-$, and •O_2^- dominated the radical oxidation process, and $^1O_2$ took part in non-radical oxidation, which synergistically favored the degradation of CBZ. Importantly, N,Fe-CDs coupled photogenerated electrons with ligand-to-metal charge transfer (LMCT) to accelerate surface Fe(III)/Fe(II) cycling, thereby sustaining PMS activation under mildly acidic to neutral conditions. HPLC-MS/MS analysis identified 14 key degradation intermediates. Combined with density-functional theory (DFT) calculations, it was revealed that hydroxylation, ring-opening, and dehydrogenation reactions preferentially occur at the seven-membered azacyclic ring of CBZ. T.E.S.T toxicity prediction indicated that the system effectively degrades CBZ into less toxic products.

CRediT authorship contribution statement

Weiwei Yu: Conceptualization, Funding acquisition, Supervision, Writing review & editing. **Beiyan Li**: Data curation, Investigation, Writing original draft. **Sikai Zhao**: Methodology, Formal analysis. **Chuandong Tang**: Investigation, Validation. **Bolin Li**: Validation, Software. **Feng Yu**: Writing review & editing. **Yuanxin Liu**: Software. **Ji Li**: Validation. **Xinyan Li**: Software. **Dan Liu**: Software. **Yan Luo:** Validation.

Declaration of Competing Interest

The authors declare that they have no known competing financial interests or personal relationships that could have appeared to influence the work reported in this paper.

Data availability

Data will be made available on request.

Acknowledgements

This work was supported by Science and Technology Research Program of Chongqing Municipal Education Commission (Grant No. KJQN202404306), (Grant No. KJQN202504326) and the Chongqing Postgraduate Joint Training Base Construction Project (Grant No. JDLHPYJD2022005).

Supporting information

The detailed experimental information is described in the Support Information.

References

Ahmad, S., Liu, L.A., Zhang, S.C., Tang, J.C., (2023). Nitrogen-doped biochar (N-doped BC) and iron/nitrogen co-doped biochar (Fe/N co-doped BC) for removal of refractory organic pollutants. Journal of Hazardous Materials 446. https://10.1016/j.jhazmat.2023.130727

Ahmadian-Fard-Fini, S., Ghanbari, D., Amiri, O., Salavati-Niasari, M., (2021). Green sonochemistry assisted synthesis of hollow magnetic and photoluminescent MgFe2O4-carbon dot nanocomposite as a sensor for toxic Ni(ii), Cd(ii) and Hg(ii) ions and bacteria. Rsc Advances 11(37), 22805-22811. https://10.1039/d1ra02458b

Ahmed, M.M., Brienza, M., Goetz, V., Chiron, S., (2014). Solar photo-Fenton using peroxymonosulfate for organic micropollutants removal from domestic wastewater: Comparison with heterogeneous TiO2 photocatalysis. Chemosphere 117, 256-261. https://10.1016/j.chemosphere.2014.07.046

Al-Qahtani, S.D., Hameed, A., Snari, R.M., Shah, R., Alfi, A.A., Shaaban, F., El-Metwaly, N.M., (2022). Development of fluorescent carbon dots ink from rice straw waste toward security authentication. Journal of Molecular Liquids 354. https://10.1016/j.molliq.2022.118927

Ali, F., Khan, J.A., Shah, N.S., Sayed, M., Khan, H.M., (2018). Carbamazepine degradation by UV and UV-assisted AOPs: Kinetics, mechanism and toxicity investigations. Process Safety and Environmental Protection 117, 307-314. https://10.1016/j.psep.2018.05.004

Almeida, A., Soares, A., Esteves, V.I., Freitas, R., (2021). Occurrence of the antiepileptic carbamazepine in water and bivalves from marine environments: A review. Environmental Toxicology and Pharmacology 86. https://10.1016/j.etap.2021.103661

Bourlinos, A.B., Rathi, A.K., Gawande, M.B., Hola, K., Goswami, A., Kalytchuk, S., Karakassides, M.A., Kouloumpis, A., Gournis, D., Deligiannakis, Y., Giannelis, E.P., Zboril, R., (2017). Fe(III)-functionalized carbon dots Highly efficient photoluminescence redox catalyst for hydrogenations of olefins and decomposition of hydrogen peroxide. Applied Materials Today 7, 179-184. https://10.1016/j.apmt.2017.03.002

Brezina, E., Prasse, C., Meyer, J., Mückter, H., Ternes, T.A., (2017). Investigation and risk evaluation of the occurrence of carbamazepine, oxcarbazepine, their human metabolites and transformation products in the urban water cycle. Environmental Pollution 225, 261-269. https://10.1016/j.envpol.2016.10.106

Bu, L.J., Zhou, S.Q., Zhu, S.M., Wu, Y.T., Duan, X.D., Shi, Z., Dionysiou, D.D., (2018). Insight into carbamazepine degradation by UV/monochloramine: Reaction mechanism, oxidation products, and DBPs formation. Water Research 146, 288-297. https://10.1016/j.watres.2018.09.036

Cai, A.H., Deng, J., Zhu, T.X., Ye, C., Li, J., Zhou, S.Q., Li, Q.S., Li, X.Y., (2021). Enhanced oxidation of carbamazepine by UV-

LED/persulfate and UV-LED/H2O2 processes in the presence of trace copper ions. Chemical Engineering Journal 404. https://10.1016/j.cej.2020.127119

Chang, C.Y., Kashale, A.A., Lee, C.M., Chu, S.L., Lin, Y.F., Chen, I.W.P., (2021). Single atomically anchored iron on graphene quantum dots for a highly efficient oxygen evolution reaction. Materials Today Energy 20. https://10.1016/j.mtener.2021.100693

Chen, H., Wang, X., Bi, W., Wu, Y., Dong, W., (2017). Photodegradation of carbamazepine with BiOCl/Fe3O4 catalyst under simulated solar light irradiation. Journal of Colloid and Interface Science 502, 89-99. https://doi.org/10.1016/j.jcis.2017.04.031

Chen, Y., Zhang, K., Zuo, Y.G., (2013). Direct and indirect photodegradation of estriol in the presence of humic acid, nitrate and iron complexes in water solutions. Science of the Total Environment 463, 802-809. https://10.1016/j.scitotenv.2013.06.026

Di, J., Xia, J.X., Ge, Y.P., Li, H.P., Ji, H.Y., Xu, H., Zhang, Q., Li, H.M., Li, M.N., (2015). Novel visible-light-driven CQDs/Bi2WO6 hybrid materials with enhanced photocatalytic activity toward organic pollutants degradation and mechanism insight. Applied Catalysis B-Environmental 168, 51-61. https://10.1016/j.apcatb.2014.11.057

Ding, Y.B., Zhang, G.L., Wang, X.R., Zhu, L.H., Tang, H.Q., (2017). Chemical and photocatalytic oxidative degradation of carbamazepine by using metastable Bi3+ self-doped NaBiO3 nanosheets as a bifunctional material. Applied Catalysis B-Environmental 202, 528-538. https://10.1016/j.apcatb.2016.09.054

Dong, H.Y., Xu, Q.H., Lian, L.S., Li, Y., Wang, S.C., Li, C., Guan, X.H., (2021). Degradation of Organic Contaminants in the Fe(II)/Peroxymonosulfate Process under Acidic Conditions: The Overlooked Rapid Oxidation Stage. Environmental Science & Technology 55(22), 15390-15399. https://10.1021/acs.est.1c04563

Fan, J.H., Gu, L., Wu, D.L., Liu, Z.G., (2018). Mackinawite (FeS) activation of persulfate for the degradation of p-chloroaniline: Surface reaction mechanism and sulfur-mediated cycling of iron species. Chemical Engineering Journal 333, 657-664. https://10.1016/j.cej.2017.09.175

Ghauch, A., Baydoun, H., Dermesropian, P., (2011). Degradation of aqueous carbamazepine in ultrasonic/Fe0/H2O2 systems. Chemical Engineering Journal 172(1), 18-27. https://10.1016/j.cej.2011.04.002

Gholizade, A., Asadollahfardi, G., Rezaei, R., (2023). Reactive Blue 19 dye removal by UV-LED/chlorine advanced oxidation process. Environmental Science and Pollution Research 30(1), 1704-1718. https://10.1007/s11356-022-22273-9

Huang, X., Lu, G., Zhu, X., Pu, C., Guo, J., Liang, X., (2024). Insight into the generation of toxic by-products during UV/H2O2 degradation of carbamazepine: Mechanisms, N-transformation and toxicity. Chemosphere 358, 142175. https://doi.org/10.1016/j.chemosphere.2024.142175

Huie, R.E., Ross, A.B.J.J.o.P., Data, C.R., (1988). Rate constants for reactions of inorganic radicals in aqueous solution. 17(3), 1027-1284.

Jiang, L.B., Xie, S.R., Chen, H.Y., Yang, J.J., Wang, X.Y., Li, W.Q., Peng, X., Wu, Z.B., Wang, H., Wang, J.J., Yuan, X.Z., (2025). Visible-light-promoted peroxymonosulfate activation for ACE degradation: Overlooked role of photogenerated hole. Applied Catalysis B-Environment and Energy 365. https://10.1016/j.apcatb.2024.124881

Kang, Y.M., Kim, M.K., Zoh, K.D., (2018). Effect of nitrate, carbonate/bicarbonate, humic acid, and H2O2 on the kinetics and degradation mechanism of Bisphenol-A during UV photolysis. Chemosphere 204, 148-155. https://10.1016/j.chemosphere.2018.04.015

Li, H., Yang, Y.L., Li, X., Zhou, Z.W., Feng, J.Y., Dai, Y.N., Li, X.H., Ren, J.W., (2022). Degradation of sulfamethazine by vacuum ultraviolet-activated sulfate radical-advanced oxidation: efficacy, mechanism and influences of water constituents. Separation and Purification Technology 282. https://10.1016/j.seppur.2021.120058

Li, H.C., Shan, C., Pan, B.C., (2018). Fe(III)-Doped g-C3N4 Mediated Peroxymonosulfate Activation for Selective Degradation of Phenolic Compounds via High-Valent Iron-Oxo Species. Environmental Science & Technology 52(4), 2197-2205. https://10.1021/acs.est.7b05563

Li, Q.S., Lu, H., Wang, X.L., Hong, Z.Q., Fu, Z., Liu, X.X., Zhou, J.T., (2022). Visible-light-driven N and Fe co-doped carbon dots for peroxymonosulfate activation and highly efficient aminopyrine photodegradation. Chemical Engineering Journal 443. https://10.1016/j.cej.2022.136473

Li, X., Wang, S.W., Xu, B.K., Zhang, X., Xu, Y.H., Yu, P., Sun, Y.J., (2022). MOF etching-induced Co-doped hollow carbon nitride catalyst for efficient removal of antibiotic contaminants by enhanced perxymonosulfate activation. Chemical Engineering Journal 441. https://10.1016/j.cej.2022.136074

Liang, C., Su, H.-W., (2009). Identification of Sulfate and Hydroxyl Radicals in Thermally Activated Persulfate. Industrial & Engineering Chemistry Research 48(11), 5558-5562. https://10.1021/ie9002848

Lim, S.Y., Shen, W., Gao, Z., (2015). Carbon quantum dots and their applications. Chem Soc Rev 44(1), 362-381. https://10.1039/c4cs00269e

Ling, C., Li, C.L., Liang, A.P., Wang, W.H., (2023). Efficient degradation of polyethylene microplastics with VUV/UV/PMS: The critical role of VUV and mechanism. Separation and Purification Technology 316. https://10.1016/j.seppur.2023.123812

Ling, L., Zhang, D.P., Fan, C.H., Shang, C., (2017). A Fe(II)/citrate/UV/PMS process for carbamazepine degradation at a very low Fe(II)/PMS ratio and neutral pH: The mechanisms. Water Research 124, 446-453. https://10.1016/j.watres.2017.07.066

Liu, N., Lu, N., Yu, H.T., Chen, S., Quan, X., (2021). Degradation of aqueous bisphenol A in the CoCN/Vis/PMS system: Catalyst design, reaction kinetic and mechanism analysis. Chemical Engineering Journal 407. https://10.1016/j.cej.2020.127228

Liu, S., Zhao, C., Wang, Z.Y., Ding, H.J., Deng, H.P., Yang, G., Li, J.F., Zheng, H.L., (2020). Urea-assisted one-step fabrication of a novel nitrogen-doped carbon fiber aerogel from cotton as metal-free catalyst in peroxymonosulfate activation for efficient degradation of carbamazepine. Chemical Engineering Journal 386. https://10.1016/j.cej.2020.124015

Liu, Y.L., Deng, P.J., Wu, R.Q., Zhang, X.L., Sun, C.H., Li, H.T., (2021). Oxygen vacancies for promoting the electrochemical nitrogen reduction reaction. Journal of Materials Chemistry A 9(11), 6694-6709. https://10.1039/d0ta11522c

Miao, S.H., Liang, K., Zhu, J.J., Yang, B., Zhao, D.Y., Kong, B., (2020). Hetero-atom-doped carbon dots: Doping strategies, properties and applications. Nano Today 33. https://10.1016/j.nantod.2020.100879

Mir, T.U., Shukla, S., Malik, A.Q., Singh, J., Kumar, D., (2023). Microwave-assisted synthesis of N-doped carbon quantum dots for detection of methyl orange in saffron. Chemical Papers 77(7), 3641-3649. https://10.1007/s11696-023-02726-2

Rahmani, Z., Ghaemy, M., (2019). One-step hydrothermal-assisted synthesis of highly fluorescent N-doped carbon dots from gum tragacanth: Luminescent stability and sensitive probe for Au3+ ions. Optical Materials 97. https://10.1016/j.optmat.2019.109356

Rodríguez-Chueca, J., Garcia-Cañibano, C., Sarro, M., Encinas, A., Medana, C., Fabbri, D., Calza, P., Marugán, J., (2019). Evaluation of transformation products from chemical oxidation of micropollutants in wastewater by photoassisted generation of sulfate radicals. Chemosphere 226, 509-519. https://10.1016/j.chemosphere.2019.03.152

Rosso, C., Filippini, G., Prato, M., (2020). Carbon Dots as Nano-Organocatalysts for Synthetic Applications. Acs Catalysis 10(15), 8090-8105. https://10.1021/acscatal.0c01989

Santoke, H., Song, W.H., Cooper, W.J., Peake, B.M., (2012). Advanced oxidation treatment and photochemical fate of selected antidepressant pharmaceuticals in solutions of Suwannee River humic acid. Journal of Hazardous Materials 217, 382-390. https://10.1016/j.jhazmat.2012.03.049

Shahzad, A., Jawad, A., Ifthikar, J., Chen, Z.L., Chen, Z.Q., (2019). The hetero-assembly of reduced graphene oxide and hydroxide nanosheets as superlattice materials in PMS activation. Carbon 155, 740-755. https://10.1016/j.carbon.2019.09.033

Shi, R., Li, Z., Yu, H.J., Shang, L., Zhou, C., Waterhouse, G.I.N., Wu, L.Z., Zhang, T.R., (2017). Effect of Nitrogen Doping Level on the Performance of N-Doped Carbon Quantum Dot/TiO2 Composites for Photocatalytic Hydrogen Evolution. Chemsuschem 10(22), 4650-4656. https://10.1002/cssc.201700943

Song, H., Li, Y.G., Lou, Z.R., Xiao, M., Hu, L., Ye, Z.Z., Zhu, L.P., (2015). Synthesis of Fe-doped WO3 nanostructures with high visible-light-driven photocatalytic activities. Applied Catalysis B-Environmental 166, 112-120. https://10.1016/j.apcatb.2014.11.020

Stefánsson, A., (2007). Iron(III) Hydrolysis and Solubility at 25 °C. Environmental Science & Technology 41(17), 6117-6123. https://10.1021/es070174h

Tian, M.S., Hu, C.Y., Yu, J.X., Chen, L.G., (2023). Carbon quantum dots (CQDs) mediated Z-scheme g-C3N4-CQDs/BiVO4 heterojunction with enhanced visible light photocatalytic degradation of Paraben. Chemosphere 323. https://10.1016/j.chemosphere.2023.138248

Wang, F.L., Chen, P., Feng, Y.P., Xie, Z.J., Liu, Y., Su, Y.H., Zhang, Q.X., Wang, Y.F., Yao, K., Lv, W.Y., Liu, G.G., (2017). Facile synthesis of N-doped carbon dots/g-C3N4 photocatalyst with enhanced visible-light photocatalytic activity for the degradation of indomethacin. Applied Catalysis B-Environmental 207, 103-113. https://10.1016/j.apcatb.2017.02.024

Wang, S., Wang, Z., (2017). Elucidating Direct Photolysis Mechanisms of Different Dissociation Species of Norfloxacin in Water and Mg2+ Effects by Quantum Chemical Calculations. Molecules 22(11). https://10.3390/molecules22111949

Wang, S.L., Zhou, N., (2016). Removal of carbamazepine from aqueous solution using sono-activated persulfate process. Ultrasonics Sonochemistry 29, 156-162. https://10.1016/j.ultsonch.2015.09.008

Wang, Y., Hu, A., (2014). Carbon quantum dots: synthesis, properties and applications. Journal of Materials Chemistry C 2(34). https://10.1039/c4tc00988f

Wang, Z., Qiu, W., Pang, S.Y., Guo, Q., Guan, C.T., Jiang, J., (2022). Aqueous Iron(IV)-Oxo Complex: An Emerging Powerful Reactive Oxidant Formed by Iron(II)-Based Advanced Oxidation Processes for Oxidative Water Treatment. Environmental Science & Technology 56(3), 1492-1509. https://10.1021/acs.est.1c04530

Wang, Z., Srivastava, V., Wang, S., Sun, H., Thangaraj, S.K., Jänis, J., Sillanpää, M., (2020). UVC-assisted photocatalytic degradation of carbamazepine by Nd-doped Sb2O3/TiO2 photocatalyst. Journal of Colloid and Interface Science 562, 461-469. https://doi.org/10.1016/j.jcis.2019.11.094

Wu, N.N., Cao, W.M., Qu, R.J., Zhou, D.M., Sun, C., Wang, Z.Y., (2021). Photochemical transformation of decachlorobiphenyl (PCB-209) on the surface of microplastics in aqueous solution. Chemical Engineering Journal 420. https://10.1016/j.cej.2021.129813

Yang, B., Kookana, R.S., Williams, M., Du, J., Doan, H., Kumar, A., (2016). Removal of carbamazepine in aqueous solutions through solar photolysis of free available chlorine. Water Research 100, 413-420. https://10.1016/j.watres.2016.05.048

Yang, Y.Y., Chen, G.J., Yu, J., He, M., An, M.Z., Lei, T., Qin, Q.Q., Qin, S.H., (2024). Fe, N-doped carbon dots/RF in self-Fenton cascade reaction: Improved photodegradation mechanism and toxicity evaluation. Journal of Environmental Chemical Engineering 12(6). https://10.1016/j.jece.2024.114151

Yentür, G., Dükkanci, M., (2020). Synthesis of Visible-Light heterostructured photocatalyst of Ag/AgCl deposited on (040) facet of monoclinic BiVO4 for efficient carbamazepine photocatalytic removal. Applied Surface Science 531. https://10.1016/j.apsusc.2020.147322

Zeng, H.X., Zhu, H., Deng, J., Shi, Z., Zhang, H.J., Li, X.Y., Deng, L., (2022). New insight into peroxymonosulfate activation by CoAl-LDH derived CoOOH: Oxygen vacancies rather than Co species redox pairs induced process. Chemical Engineering Journal 442. https://10.1016/j.cej.2022.136251

Zeng, T., Xia, S.S., Li, S.Q., Hong, X.X., Wang, Y.S., Wang, L.T., Huang, X.W., (2023). Kinetic and mechanistic investigations of the oxidation of organics by near-infrared light driven thermocatalytic activation of peroxydisulfate with Fe3O4. Chemical Engineering Journal 455. https://10.1016/j.cej.2022.140629

Zhang, T.T., Zhao, Y.L., Kang, S.C., Li, Y.J., Zhang, Q.W., (2019). Formation of active Fe(OH)3 in situ for enhancing arsenic removal from water by the oxidation of Fe(II) in air with the presence of CaCO3. Journal of Cleaner Production 227, 1-9. https://10.1016/j.jclepro.2019.04.199

Zhang, W., Li, M., Luo, J.W., Zhang, G., Lin, L., Sun, F.Y., Li, M., Dong, Z.J., Li, X.Y., (2023). Modulating the coordination environment of Co single-atom catalysts through sulphur doping to efficiently enhance peroxymonosulfate activation

for degradation of carbamazepine. Chemical Engineering Journal 474. https://10.1016/j.cej.2023.145377

Zhang, X., Liao, X., Hou, Y., Jia, B., Fu, L., Jia, M., Zhou, L., Lu, J., Kong, W., (2022). Recent advances in synthesis and modification of carbon dots for optical sensing of pesticides. Journal of Hazardous Materials 422, 126881. https://doi.org/10.1016/j.jhazmat.2021.126881

Zhang, Y., Geißen, S.-U., Gal, C., (2008). Carbamazepine and diclofenac: Removal in wastewater treatment plants and occurrence in water bodies. Chemosphere 73(8), 1151-1161. https://doi.org/10.1016/j.chemosphere.2008.07.086

Zhang, Y., Wang, Y.L., Feng, X.T., Zhang, F., Yang, Y.Z., Liu, X.G., (2016). Effect of reaction temperature on structure and fluorescence properties of nitrogen-doped carbon dots. Applied Surface Science 387, 1236-1246. https://10.1016/j.apsusc.2016.07.048

Zhao, G., Zou, J., Chen, X., Liu, L., Wang, Y., Zhou, S., Long, X., Yu, J., Jiao, F., (2021). Iron-based catalysts for persulfate-based advanced oxidation process: Microstructure, property and tailoring. Chemical Engineering Journal 421, 127845. https://doi.org/10.1016/j.cej.2020.127845

Zhao, G.Q., Zou, J., Chen, X.Q., Liu, L.K., Wang, Y.K., Zhou, S., Long, X.Q., Yu, J.G., Jiao, F.P., (2021). Iron-based catalysts for persulfate-based advanced oxidation process: Microstructure, property and tailoring. Chemical Engineering Journal 421. https://10.1016/j.cej.2020.127845

Zhou, Y., Jiang, J., Gao, Y., Pang, S.Y., Ma, J., Duan, J.B., Guo, Q., Li, J., Yang, Y., (2018). Oxidation of steroid estrogens by peroxymonosulfate (PMS) and effect of bromide and chloride ions: Kinetics, products, and modeling. Water Research 138, 56-66. https://10.1016/j.watres.2018.03.045

Zhu, X.B., Li, H., Shang, X.H., He, T.F., (2022). Fe-Cu binary oxide loaded zeolite as heterogeneous Fenton catalyst for degradation of carbamazepine at near-neutral pH. Environmental Science and Pollution Research 29(48), 73181-73190. https://10.1007/s11356-022-20299-7

Supporting Information

Text S1. Detection of Fe(II)

In this study, we refer to the method of the Chinese national standard "Water quality - Determination of iron - o-phenanthroline spectrophotometric method (for trial use)" (HJ/T 345-2007), which was used to monitor the concentration of Fe(II) and its dynamic changes in the reaction system(Guo *et al.*, 2013). The specific experimental steps are as follows:

First, the standard iron solution was transferred into a conical flask, and ultrapure water, 1 mL of hydrochloric acid (VHCl/VH_2O=1/3 by volume), and 1 mL of 10% hydroxylamine hydrochloride were added, mixed, and then heated and concentrated to approximately 15 mL. The concentrated solution was then transferred to a 50 mL cuvette containing Congo red indicator, and saturated sodium acetate was added dropwise until the test paper turned red to adjust the acidity. Next, 2.5 mL of buffer solution and 1 mL of 0.5% o-phenanthroline solution were added sequentially, and the final volume was made up to 25 mL with ultrapure water to develop the color. The absorbance was measured at 510 nm to establish the standard curve of Fe(II). The detection range of this method was 0.02-5.00 mg/L, and the fitted correlation coefficient R^2 was more than 0.999. The fitted equation is shown in Eq. S1.

During the analysis of the samples, 0.5 mL of reaction solution was taken from the degradation system at different time points and filtered through a 0.22 μm nylon membrane to remove the particles, then 2.5 mL of acetic acid/ammonium acetate buffer and 1 mL of 0.5% o-phenanthroline were added to the filtrate and the solution was fixed to 25 mL, and then mixed thoroughly and analyzed by colorimetric analysis. The resulting absorbance was used to calculate the actual concentration of Fe(II) in the solution. The amount of photogenerated Fe(II) was calculated from the difference in concentration between the experimental group (UV irradiation) and the control group (dark treatment).

$$Y = (\mathrm{x} - 0.000697952) / 0.13195 \qquad \text{Eq. S1}$$

Text S2. Detailed assay conditions for HPLC-MS/MS analysis

The degradation intermediates of CBZ were characterized by an Agilent 1100 HPLC system coupled with a Thermo TSQ Quantum Ultra AM triple quadrupole mass spectrometer (HPLC-MS/MS).

The chromatographic conditions were as follows: chromatographic column: welch Xtimate C18 (2.1×100 mm, 3 μm); testing temperature: 22°C; injection volume: 2.0 μl; UV detection wavelengths: 254 nm and 275 nm; the mobile phases consisted of A: 0.1% formic acid in water and B acetonitrile; the flow rate was 0.5 mL/min. The mass spectrometry (MS) conditions were as follows: HESI II Ion Source, positive mode. Scanning range: 50-550 M/z.

Table S1. HPLC-MS/MS gradient elution procedure

Time(min)	A%	B%
0	98	2
8	6	94
10.50	6	94
10.51	98	2

Table S2. Transformation products of CBZ in UV/N,Fe-CDs/PMS system.

Product number	Time(min)	m/z	Pseudo-molecular formula	Structural formula
CBZ	5.60	237	$C_{15}H_{12}N_2O$	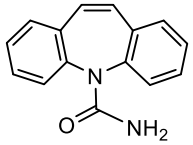

P1	4.53	253	$C_{15}H_{12}N_2O_2$	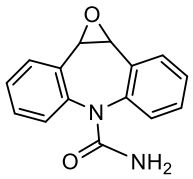
P2	6.69	271	$C_{15}H_{14}N_2O_3$	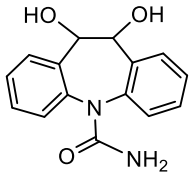
P3	4.39	273	$C_{15}H_{16}N_2O_3$	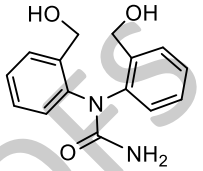
P4	4.20	269	$C_{15}H_{12}N_2O_3$	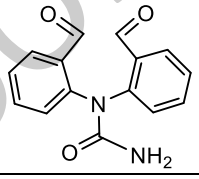
P5	4.78	267	$C_{15}H_{10}N_2O_3$	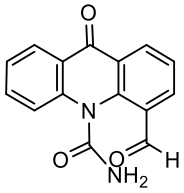
P6	4.95	283	$C_{15}H_{10}N_2O_4$	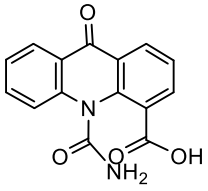
P7	4.79	224	$C_{14}H_9NO_2$	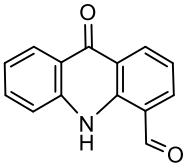
P8	5.71	196	$C_{13}H_9NO$	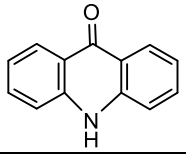
P9	5.43	287	$C_{15}H_{14}N_2O_4$	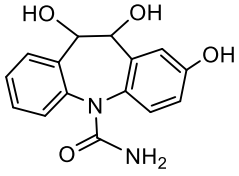
P10	5.78	255	$C_{15}H_{12}N_2O_2$	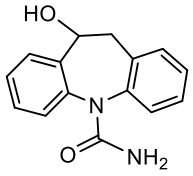

P11	5.36	251	$C_{15}H_{10}N_2O_2$	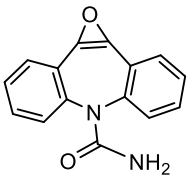
P12	4.05	210	$C_{14}H_{11}NO$	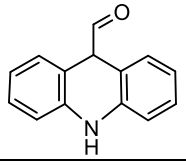
P13	4.98	180	$C_{13}H_9N$	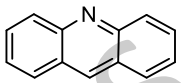
P14	4.98	198	$C_{13}H_{11}NO$	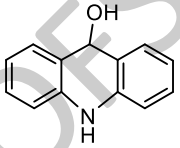

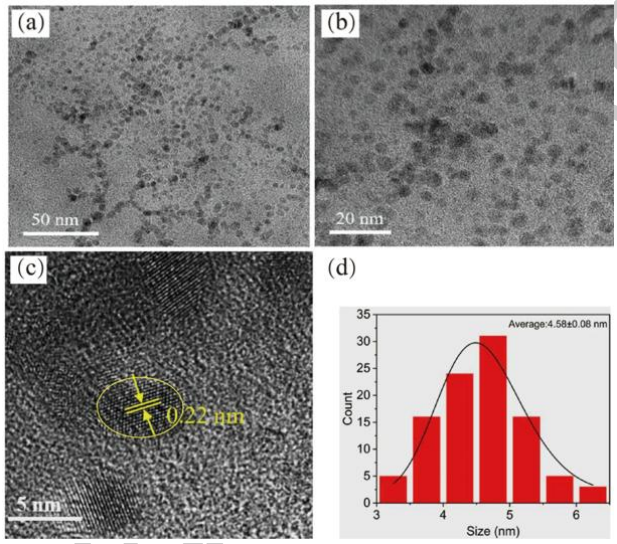

Figure S1. (a-b) TEM images Fof N,Fe-CDs; (c) HR-TEM image of N,Fe-CDs; (d) Particle size distribution of N,Fe-CDs;

References

Guo Y, Lou X, Fang C, Xiao D, Wang Z, Liu J (2013). Novel Photo-Sulfite System: Toward Simultaneous Transformations of Inorganic and Organic Pollutants. *Environmental Science & Technology*, 47(19): 11174–11181